



ELSEVIER

Contents lists available at [ScienceDirect](https://www.sciencedirect.com)

Mechanism and Machine Theory

journal homepage: www.elsevier.com/locate/mechmt

Assessment of pantograph-catenary interaction in a railway overlap section via a novel optical-based method

Tengjiao Jiang^{*}, Gunnstein T. Frøseth, Petter Nåvik, Anders Rønquist

Department of Structural Engineering, Norwegian University of Science and Technology, Rich. Birkelands vei 1A, 7491 Trondheim, Norway

ARTICLE INFO

Keywords:

Railway catenary system
Pantograph-catenary interaction
Section overlap
Computer vision
Displacement measurement

ABSTRACT

Smooth pantograph-catenary contact is essential for regular train operation. However, catenary section overlaps are locations where peak contact forces occur, which significantly affects current collection quality. This work studies pantograph-catenary interaction and transition at an existing overlap span by using a novel optical-based measuring method. Image sequences of eleven single- and two double-pantograph train passages were processed to obtain wire displacement responses. The unsynchronised vibration of two contact wires was found, and the first contact wire exhibits different modal responses. The spatial motion paths of contact wires were obtained to estimate the pantograph-catenary interaction. Dynamic effects rendering high contact forces, contact loss and arcing were investigated. The results show that pantographs with a long transition distance and a high intersection gradient cause a serve impulse with the second contact wire, resulting in contact loss and arcing. Finally, this study successfully estimated the transition distance and found it has a strong positive correlation with peak contact forces and train speeds. The transition distance exhibits an increasing tendency with increasing train speed. The longer transition distance results in a higher peak contact force.

1. Introduction

Most high-speed trains in operation are powered by electricity because diesel locomotives are essentially unable to generate enough energy to reach high speeds [1]. Electricity is delivered through the pantograph-catenary system, composed of pantographs and flexible catenary wires [2]. The pantograph mounted atop a train occurs in sliding contact with a contact wire to collect an electrical current [3]. The main structural components of the catenary system include contact and messenger wires, droppers and occasionally stitch wires [4]. The messenger wire is suspended by cantilevers from poles at regular intervals. The main task of the messenger wire is to hang the contact wire to the required design height from the track, achieved by droppers clamped onto the messenger and contact wires [5]. The contact wire follows a zigzag pattern to ensure that the sliding contact point moves over the panhead from side to side to distribute wear [6].

High speeds increase the dynamic response of the catenary system due to higher interaction forces. A smooth contact between the contact wires and pantograph is essential for regular train operation [7]. A good pantograph-catenary contact improves the current collection quality, minimises contact loss and reduces wear. However, contact loss is a significant issue in pantograph-catenary interaction since it interrupts the power supply and increases wear [8].

Overlapping sections are considered one of the most critical parts of ensuring the current collection quality [9–11]. Each catenary

^{*} Corresponding author at: Richard Birkelands vei 1A, 7491 Trondheim, Norway.
E-mail address: tj.jiang@outlook.com (T. Jiang).

<https://doi.org/10.1016/j.mechmachtheory.2022.105045>

Received 29 April 2022; Received in revised form 4 July 2022; Accepted 24 July 2022

Available online 1 August 2022

0094-114X/© 2022 The Author(s). Published by Elsevier Ltd. This is an open access article under the CC BY license (<http://creativecommons.org/licenses/by/4.0/>).

Nomenclature

a	acceleration of the contact wire
CMOS	complementary metal-oxide-semiconductor sensor
D_w	object distance between the camera and objects
D_h	the horizontal distance between the camera and objects
F	the magnitude of the contact force
f	the focal length of the optical lens
H	height of measuring points from the rail surface
h_{Fj}	static height of the tracking point j on the first contact wire
h_{Sj}	static height of the tracking point j on the second contact wire
i	image serial number
j	tracking point number
L	longitudinal distance from each tracking point to the first tracking point
l_j	longitudinal distance of the tracking point j
LiDAR	light detection and ranging
m	mass of the catenary system
P_0	the measuring point at the contact wire
P_1	the measuring point at the rail
ROI	region of interest
S_c	the physical pixel size of the image sensor
SSD	solid-state drive
t	the time moment of each image
VIBLITE	a vision-based line-tracking system
x	x- image coordinate of objects
y	y- image coordinate of objects
α	the pitch angle of the camera optical axis
β	angle $\angle P_0^{prime} O I_c$
γ	pitch angle from the optical centre to the rail
Δt	the time interval between each image
θ	pitch angle from the optical centre to the contact wire
μ_i	μ - image coordinate of the crossing point
σ_i	σ - image coordinate of the crossing point
φ_i^{Fj}	uplift response of the tracking point j at the image i on the first contact wire
φ_i^{Sj}	uplift response of the tracking point j at the image i on the second contact wire

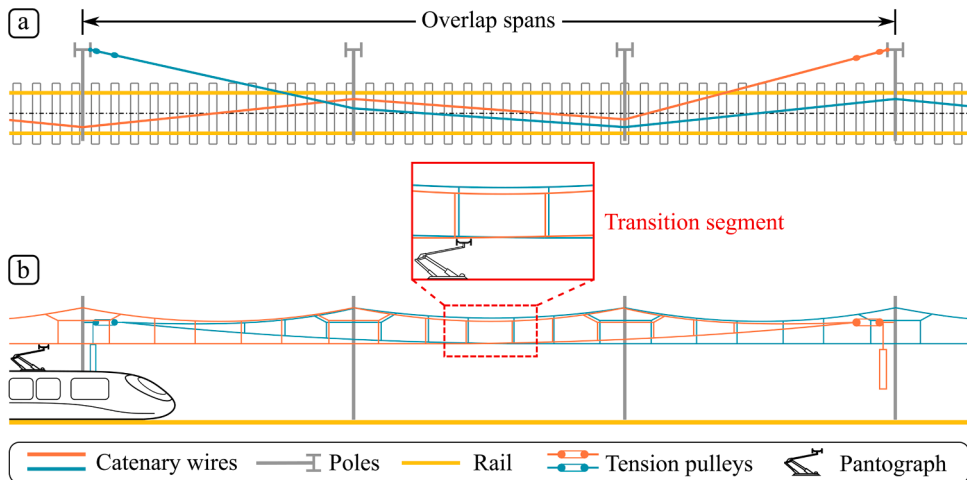


Fig. 1. A three-span overlap section of a railway catenary system. (a) Top view of the overlap section. (b) Horizontal view.

section exhibits a limited length of approximately 1-1.5 km due to the thermal expansion and tension decrease at each cantilever [12]. Tensioning devices consist of weights and pulleys to guarantee a constant mechanical tension in the catenaries. Overlap spans are designed to raise the first-section contact wire while lowering that of the second section to the nominal height to ensure pantograph transit between consecutive sections. A three-span overlap section is shown in Fig. 1, where the contact wires exhibit a parabolic shape at the overlap spans. Conventional overlap sections also include four- and five-span sections [9]. The transition segment between two catenary sections occurs in the middle of the central span for three- and five-span overlap sections (Fig. 1). The first and second contact wires are parallel in the transition segment, as shown in Fig. 2. For a four-span overlap section, the transition occurs at the pole, which is a hard point and thus may yield high contact forces.

Although a smooth contact is the design goal for the overlap span, the maximum contact force often occurs in the transition [9]. In particular, a smooth transition in overlap spans is only partially achieved in regular traffic. Thus, this work aims to study the pantograph-catenary interaction in an existing overlap span to investigate why the peak contact force occurs.

Studies of pantograph-catenary interaction mostly concern conventional spans, such as modelling methodology [1,12–15], catenary wire irregularity [16,17], wave propagation analysis [18], and catenary uplift and damping measurements [19,20]. However, only a few publications focus on the overlap spans. Shimizu et al. [21] measured the contact wire height and wear to optimise the overlap section structure for high-speed Shinkansen lines. Har ell et al. [22] carried out simulations of a five-span overlap section under multiple-pantograph train operation. Their results indicated that the overlap section dynamic performance improved by lowering the lift at the support poles. Kuraoka et al. [23] studied various contact wire configurations in overlap sections with the aim of contact wire wear reduction. An improved contact wire height was found to reduce the wear by comparing simulation results and inspection vehicle data. Vesali et al. [10] designed novel control approaches for catenary systems to prevent pantograph wear and improve the contact quality at conventional spans and overlap sections. The most systematic work was performed by Gregori et al. [9]. Their work described a simulation analysis of pantograph-catenary dynamic interaction in overlap sections under double-pantograph operation. A catenary section was optimised via the application of Bayesian optimisation techniques to reduce the contact force standard deviation, including the overlap section.

To our best knowledge, no publications have measured and investigated the pantograph-catenary interaction and transition at an existing overlap span. The unsynchronised vibration of two contact wires and contact-wire height variation put an additional challenge to the stable contact of the pantograph-catenary. Thus, our work aims to study the dynamic pantograph-catenary interaction under scheduled train operations at an existing overlap span. Computer vision techniques have been implemented in many fields, e.g., bridge engineering [24–28], mechanical engineering [29–34], and railway engineering [19,35,36]. A novel vision-based measuring method is presented and implemented to simultaneously measure the dynamic response of two contact wires to study the pantograph-catenary interaction. Eleven single- and two double-pantograph train passages were acquired from field tests with train speeds. The dynamic interaction and transition of the pantograph-catenary at the overlap span are obtained and illustrated in detail. The dynamic effects rendering high contact forces, contact loss and arcing at the overlap spans were investigated. The results show that the pantograph typically contacts the second contact wire at a distance before reaching the static crossing point. The longer distance results in a larger intersection gradient of two contact wires, and the pantograph is more likely to have a larger impulse with the second contact wire.

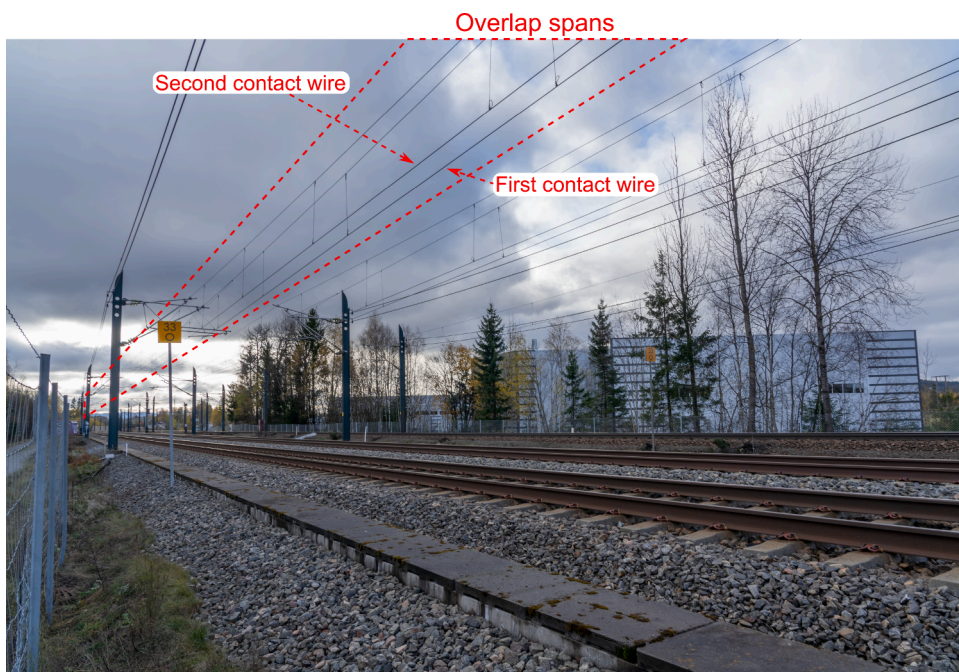


Fig. 2. Parallel contact wires in overlap spans.

This phenomenon causes contact loss and arcing. In double-pantograph train passages, the rear pantograph causes a more severe dynamic interaction than that caused by the front pantograph because of the longer transition distance, i.e., the length where the pantograph contacts with both contact wires. Finally, the transition distance was determined and assessed, and the correlation between the train speed, the transition distance and contact force was studied. The results show that they have a strong correlation, and the faster train speed would significantly increase the transition distance and apply a larger impulsive force to the second contact wire.

2. Overlap-span measurement strategy

Measuring the pantograph-catenary interaction and transition at an overlap span is a new challenge for field tests. A novel vision-based measuring method was proposed and implemented to synchronously collect the dynamic response of both contact wires and evaluate the transition. Section 2.1 details the framework of the whole measurement strategy, including static height measurement and uplift estimation, which are introduced in Sections 2.2 and 2.3, respectively.

2.1. The framework

The challenges to evaluating the pantograph-catenary interaction at the transition segment are to 1) estimate the moment when the pantograph contacts the second contact wire, 2) determine the transition segment where the pantograph contacts both contact wires and 3) measure the catenary response during the pantograph passage.

This study proposed and implemented a novel method to address the above challenges. The main idea is to 1) measure the vibration response of two contact wires simultaneously by using a vision-based system, 2) calculate the spatial motion paths of two contact wires in a world coordinate system, 3) estimate the dynamic intersection of both wires and 4) illustrate and analyse the wires' motion and the moving path of the intersection point (i.e., dynamic crossing point) in time series. Because when the pantograph contacts both wires, two contact wires will intersect at the panhead, and the contact point is also the two wires' crossing point. The motion path of the crossing point could help analyse pantograph-catenary interaction and transition.

The detailed procedure is introduced as follows:

- First, we build a world coordinate system HOL, where H is the height of measuring points from the rail surface, and L is the longitudinal distance from each tracking point to the first tracking point (S1/F1), as shown in Fig 3.
- Then, the static height of ten tracking points from the rail surface is measured by a vision-based system, expressed as $h_{F1} - h_{F5}$ and $h_{S1} - h_{S5}$ in Fig. 3(a). The longitudinal distance is also measured as $l_2 - l_5$ for each tracking point. The tracking points are usually selected as evenly distributed on both sides of the static crossing point. The measuring method based on a pinhole camera model is introduced in Section 2.2.
- Measure the dynamic uplift response of each tracking point, expressed as $\varphi_i^{F1} - \varphi_i^{F5}$ and $\varphi_i^{S1} - \varphi_i^{S5}$, as shown in Fig. 3(b). i is the image serial number. $\varphi_i^{F1} - \varphi_i^{F5}$ and $\varphi_i^{S1} - \varphi_i^{S5}$ represent the relative uplift of tracking points from the moment (image) $i-1$ to i . The displacement measuring method is mentioned in detail in Section 2.3.
- After obtaining the static height ($h_{F1} - h_{F5}$ and $h_{S1} - h_{S5}$) and dynamic uplift ($\varphi_i^{F1} - \varphi_i^{F5}$ and $\varphi_i^{S1} - \varphi_i^{S5}$), the dynamic spatial height H_i^p of each tracking point at the image i can be estimated in Eq. (1) as:

$$H_i^p = h_p + \sum_{m=0}^i \varphi_m^p \tag{1}$$

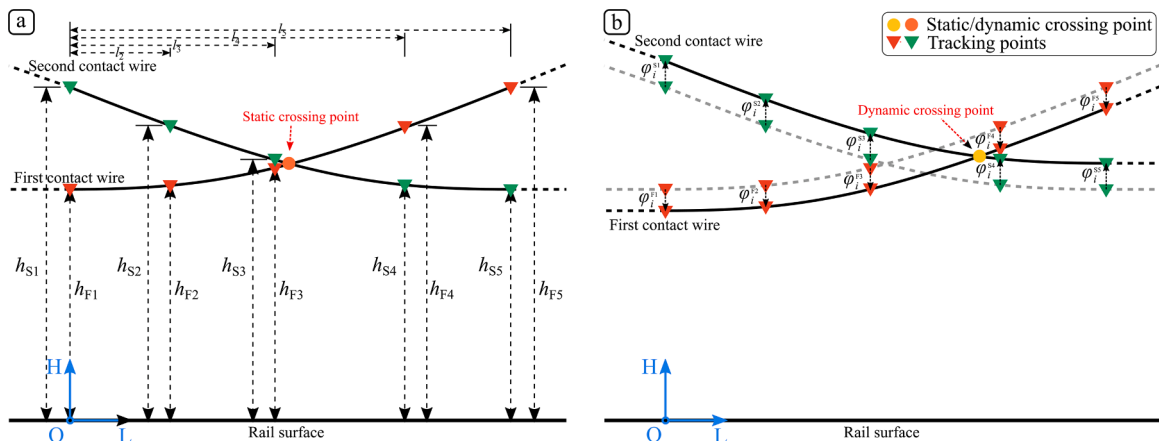


Fig. 3. Illustration of (a) static height and (b) dynamic uplift measurement of contact wires at the transition segment.

where p represents each tracking point ($p = S1-S5$ or $F1-F5$), and $\sum_{m=0}^i \phi_m^p$ means the sum of uplift response before the image i .

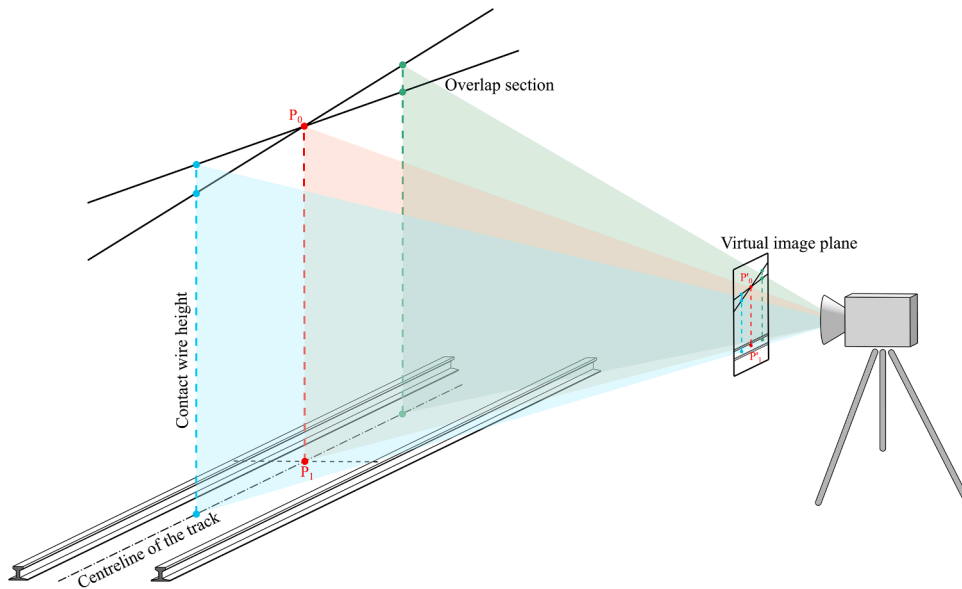
The coordinates could be obtained as (l_p, H_i^p) for each tracking point. Based on these coordinates, two fitting curves are used to fit the parabolic shape of two contact wires, as shown in Fig. 3(b). The spatial motion paths of both contact wires are then obtained. The dynamic crossing point of two contact wires is estimated at each image i , while the crossing-point coordinates (μ_i, σ_i) are variables in a time series. Finally, the motion path of the crossing point with the corresponding time t could be collected.

2.2. Geometric measurement

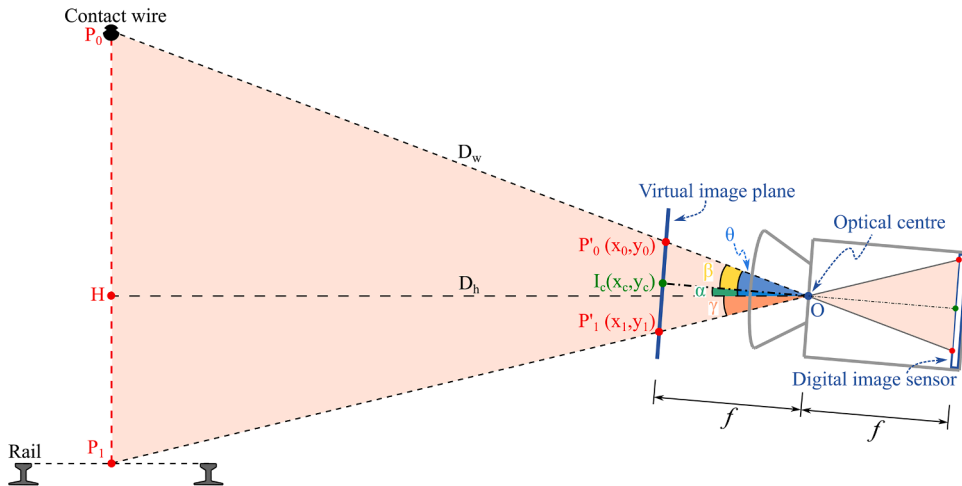
A pinhole camera model is adopted to measure the static height of the tracking points from the rail, as shown in Fig 4. The image plane is the surface of the digital image sensor. However, the resultant perspective projection of the object is inverted in the image plane. To simplify the subsequent geometric analysis, a virtual image plane is generated, which is located far from the optical centre O at focal length f . The camera pitch angle α , which always occurs after camera setup in field tests, is considered in the pinhole model to enhance the applicability.

The measuring points, i.e., P_0 at the contact wires and P_1 at the rail, are projected as P'_0 and P'_1 , respectively, in the image plane. The height P_0P_1 can be estimated as:

$$P_0P_1 = P_0H + P_1H = D_h \cdot [\tan\theta + \tan\gamma] = D_w \cdot \cos\theta \cdot [\tan\theta + \tan\gamma] \tag{2}$$



(a) Setup of the vision-based measuring system.



(b) Pinhole camera model for wire height measurement.

Fig. 4. Measuring method of the catenary wire height.

where D_w is the distance OP_0 between the contact wire and camera, and D_h is the horizontal projection OH of D_w . $\angle P_0OH$ is the pitch angle θ from the optical centre O to the contact wire P_0 , and $\angle P_1OH$ is the pitch angle γ between the optical centre O and the rail. Because D_w and θ are measured in the field with the aid of a laser rangefinder, γ is the only unknown parameter to be estimated in Eq. (4) with the pinhole camera model, starting with:

$$\begin{aligned} \angle P'_0OI_c = \beta &= \arctan\left(\frac{P'_0I_c}{OI_c}\right) = \arctan\left(\frac{\sqrt{[(x_0 - x_c)^2 + (y_0 - y_c)^2]} \cdot S_c}{f}\right) \\ \alpha &= \theta - \beta = \theta - \arctan\left(\frac{\sqrt{[(x_0 - x_c)^2 + (y_0 - y_c)^2]} \cdot S_c}{f}\right) \\ \angle P'_1OI_c = \alpha + \gamma &= \arctan\left(\frac{P'_1I_c}{OI_c}\right) = \arctan\left(\frac{\sqrt{[(x_1 - x_c)^2 + (y_1 - y_c)^2]} \cdot S_c}{f}\right) \end{aligned} \tag{3}$$

where α is the pitch angle of the optical axis, and OI_c is the focal length f of the optical lens, which is 25 mm in this case. $\angle P'_0OI_c$ is represented as β , and $P'_0(x_0, y_0)$ and $P'_1(x_1, y_1)$ are the image coordinates of the catenary wire and rail, respectively. $I_c(x_c, y_c)$ is the centre point of the image plane. Points P'_0 , P'_1 and I_c are in a straight line. S_c is the physical pixel size of the image sensor, which is 5.5 μm for the adopted camera (Basler ACA2000-165 μm). Hence, the pitch angle γ can be written as:

$$\begin{aligned} \gamma &= \angle P'_1OI_c - \alpha \\ &= \arctan\left(\frac{\sqrt{[(x_1 - x_c)^2 + (y_1 - y_c)^2]} \cdot S_c}{f}\right) + \arctan\left(\frac{\sqrt{[(x_0 - x_c)^2 + (y_0 - y_c)^2]} \cdot S_c}{f}\right) - \theta \end{aligned} \tag{4}$$

After obtaining the pitch angle γ , the catenary wire height P_0P_1 can be estimated according to Eq. (2). In this case, the scale factor of the height estimation depends on various parameters, including the catenary-wire distance D_w , pitch angle θ , image coordinates (x_0, y_0) , (x_1, y_1) and (x_c, y_c) , focal length f of the optical lens, and physical pixel size S_c of the image sensor.



Fig. 5. Wire detection challenge caused by noisy background.

Through this height estimation method, two parameters must be measured in the field tests, i.e., the catenary-wire distance D_w and pitch angle θ . The distance D_w can be measured from 0.05 to 200 m with the Leica DISTO™ D8 laser rangefinder, and the measurement accuracy, which varies between 10 and 30 m, can be controlled within 0.1 mm. Moreover, the measurement accuracy of the pitch angle θ is controlled within 0.1° . In this measurement, a 0.1 mm measuring error in D_w will cause a 1 mm error in the final height, which accounts for 0.019% of the static height of approximately 5340mm. 0.1° measuring error in θ will cause a 0.04 mm error in the final height, which is 0.00075% of the static height. Hence, the effect of any measurement errors in these two parameters on the measurement accuracy is small enough to be neglected.

2.3. Uplift measurement

A line-tracking technique [19] was adopted to identify and track wire motion from noisy backgrounds at a high sampling frequency. The open-source code has been made available in [37]. The line-tracking technique is briefly introduced in this section for completeness, and more detailed descriptions have been provided in our previous study [19].

In general, trees often occur along railways, yielding a non-uniform or noisy background of the catenary wire, which makes wire identification and tracking challenging, as shown in Fig. 5. The line-tracking technique was developed to address the essential challenge of tracking slender wires without markers against noisy backgrounds.

The line-tracking technique consists of coarse search and subpixel centreline detection. The main idea of coarse search is to employ a sliding subset to search candidate endpoints of catenary wires along with user-selected columns by comparing pixel intensity values. Blue dashed rectangles in Fig. 6 (a) represent the sliding subsets, and the left and right sides are selected as searching columns. Then, a line search is used to find the wire objects between candidate points by using another subset, shown as a red dashed rectangle in Fig. 6 (a).

Subpixel centreline detection is then performed to estimate the wire centreline through the bicubic interpolation, as shown in Fig. 6 (b). The main idea is to use the bicubic interpolation to approximate the upper and lower edges of the line object to calculate the centreline. The centreline is estimated and marked as a yellow dashed line. Finally, points on the centreline can be chosen by users to be tracking points, shown as the point P_{track} in Fig. 6 (b).

The accuracy and robustness of the line-tracking technique have been verified in [19]. The accuracy is ± 0.6 mm at the 95% confidence level with a measuring distance of 10 m, as confirmed by comparison to a laser displacement meter. The measuring error accounts for around $\pm 1\%$ of the maximum uplift of 60 mm.

3. Field tests

3.1. System configuration

A vision-based line-tracking system (VIBLITE) was adopted in the field tests, consists of two area scan cameras (Basler ACA2000-165 μm), two optical lenses with a fixed focal length (Edmund Optics 25 mm C-series), a trigger (National Instruments NI USB-6210), a solid-state drive (Samsung T7 Portable SSD 2TB), a laptop (DELL Latitude 7490) and a laser rangefinder (Leica DISTO™ D8), all shown in Fig. 7. The camera contains a complementary metal-oxide-semiconductor (CMOS) sensor with a 2048×1088 -pixel resolution. The dynamic range of the CMOS sensor is 8 bits, and the intensity value of each pixel is within the interval of [0-255]. The sensor format is 2/3 inches, the physical sensor size is 11.3×6 mm, and the physical pixel size is $5.5 \times 5.5 \mu\text{m}$. The camera is connected to the laptop

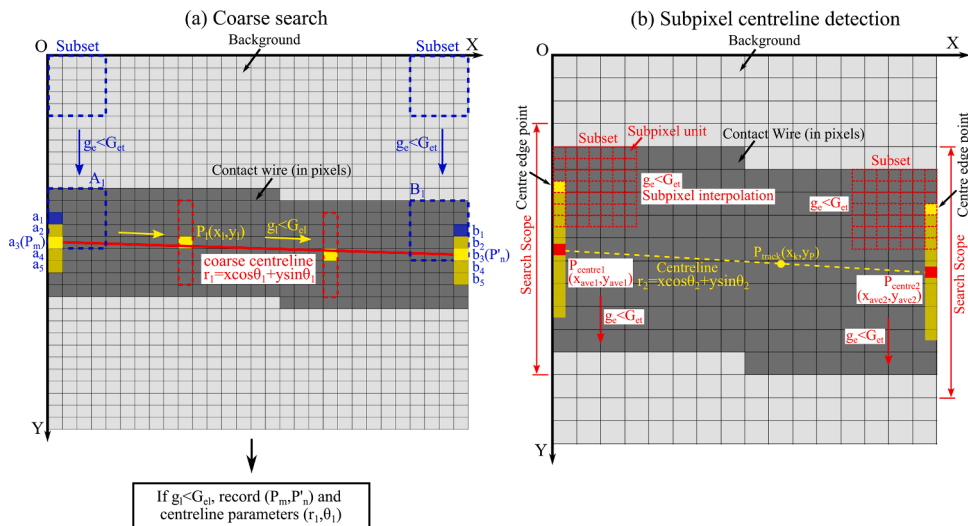


Fig. 6. The line-tracking technique consists of (a) coarse search and (b) subpixel centreline detection.

via a USB 3.0 wire for image data transmission and power supply purposes. The focal length of the lens, i.e., 25 mm, is adopted in this case. The laser rangefinder measures the catenary-wire distance D_w and pitch angle θ , both essential calibration parameters for the measured height. The laptop controls the camera sampling rate and exposure time and transfers the obtained images from the camera to the external SSD. For completeness, the weather conditions are supplemented. During the measurement, the weather was sunny, and the temperature ranged from 1–4 °C. The air humidity was approximately 75%, the wind speed was 1 m/s, and the visibility was 12.9 km.

Different catenary systems are implemented in Norway, ranging from outdated systems such as Tabell 54 to newer systems, from System 35 (130 km/h) to Systems 20 and 25 (200 km/h and 250 km/h, respectively) [38]. The current field measurements were conducted in the overlap spans along the Oslo airport line between Oslo Airport (OSL) and Oslo central station, i.e., System 25. This catenary system is a new system built and designed to accommodate trains operating at a maximum speed of 250 km/h. Two types of high-speed trains, i.e., Stadler FLIRT Class 74 and GMB Class 71 trains, run along the airport line at train speeds of 200 and 210 km/h, respectively, as shown in Fig. 7.

The five-span overlap is the standard design geometry of the Oslo airport line. The transition occurs at the midspan, where the pantograph contacts both contact wires, as shown in Fig. 1. Thus, VIBLITE was set up at the midspan to measure the transition segment, as shown in Fig. 8. Two cameras were applied to increase the longitudinal distance of the shooting regions, indicated by the blue and orange regions in Fig. 8.

3.2. Camera configurations

Because of the stitched shooting regions, one challenge of this field test is synchronising two cameras to collect the uplift response of two contact wires simultaneously, which is significant for final measuring accuracy. In the current setup, the hardware trigger (National Instruments NI USB-6210) was applied to send a logic voltage signal to synchronise two cameras' exposure to facilitate image sequence correspondence. Logic gate circuits are designed to input and output only two signal types, i.e., high (logic 1) and low (logic 0) signals, representing high and low voltage, respectively.

The exposure mode and shutter type are two essential features in camera selection. The timed and trigger-width modes are two different exposure modes (Fig. 9). Under the timed exposure mode, exposure is initiated when a high-voltage signal is detected and is maintained until the exposure time has expired. However, under the trigger width exposure mode, the exposure time is defined by the width of the high-voltage signal. This indicates that exposure is also initiated when a high-voltage signal is detected, which is only maintained until the signal falls [39]. The timed mode was employed in this case due to its advantage of controlling the exposure of each camera individually.

The shutter type is an important feature of a digital image sensor. Global and rolling shutters are two main electronic shutter types. These two shutter types entail different exposure processes and final image results, especially in regard to fast-moving objects [39].

Regarding the global shutter, the exposure of all pixels starts and ends at the same time, but readout occurs row by row. Global shutter provides non-distorted images without wobbles or skewing and is suitable for fast-moving objects, e.g., high-speed trains and vibrating catenary wires. Regarding the rolling shutter, however, exposure occurs row by row at shifted times. Thus, the rolling shutter produces image distortion for fast-moving objects.

The adopted camera (Basler ACA2000-165 μm) contains a global shutter sensor, which is suitable for the measurement of the



Fig. 7. Overlap span measurement at Oslo airport line. Photography: Tengjiao Jiang/NTNU. Maps courtesy of Kartverket©. Photos of the FLIRT train type courtesy of Norske tog© and the GMB train type courtesy of Flytoget©.

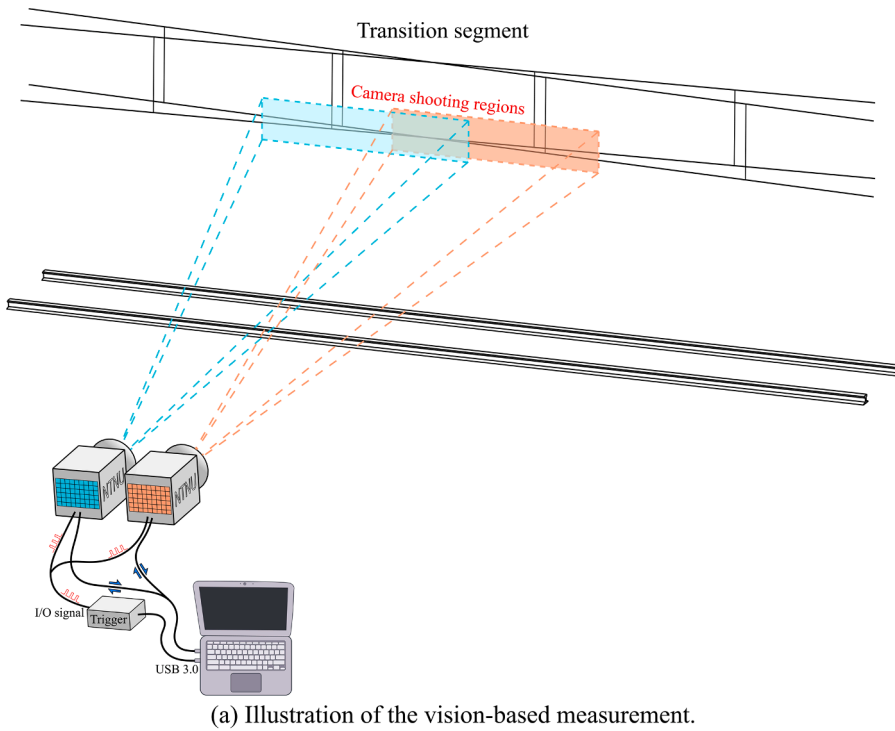


Fig. 8. Measurement schematic at the transition segment.

intense vibration of the catenary wires. A sampling frequency of 200 Hz is adopted in this field test, and the time interval is 0.005 s. The exposure time of the cameras was limited by the sampling frequency and the time for the transferral of the obtained images to the laptop, e.g., less than 5 ms at the 200-Hz sampling frequency. Due to the limitation of the USB cable transfer speed at 200 Hz, each frame was cropped, and the pixel resolution was reduced to 2048×400 pixels.

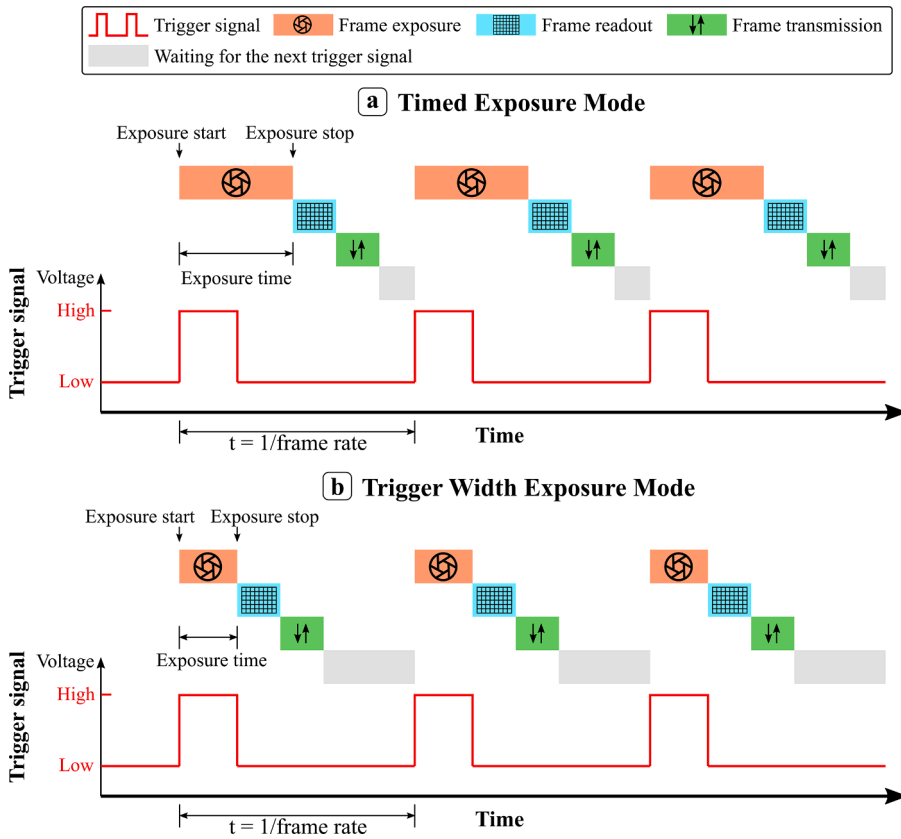


Fig. 9. Camera exposure modes.

3.3. Train-speed measuring method

A Stalker LIDAR XLR instrument was applied to measure the train speed, as shown in Fig. 10. This instrument is a small and light hand-held gun-type LiDAR and achieves a good measuring range, high accuracy, and short acquisition time. It measures targets up to 1200 m away, and speeds ranging from 2-481 km/h can be measured at an accuracy of ± 1 km/h. Thus, the train speeds of both Classes 71 and 74 (210 and 200 km/h) are well within the measuring range, and the train speed was included as a variable in the following data analysis.

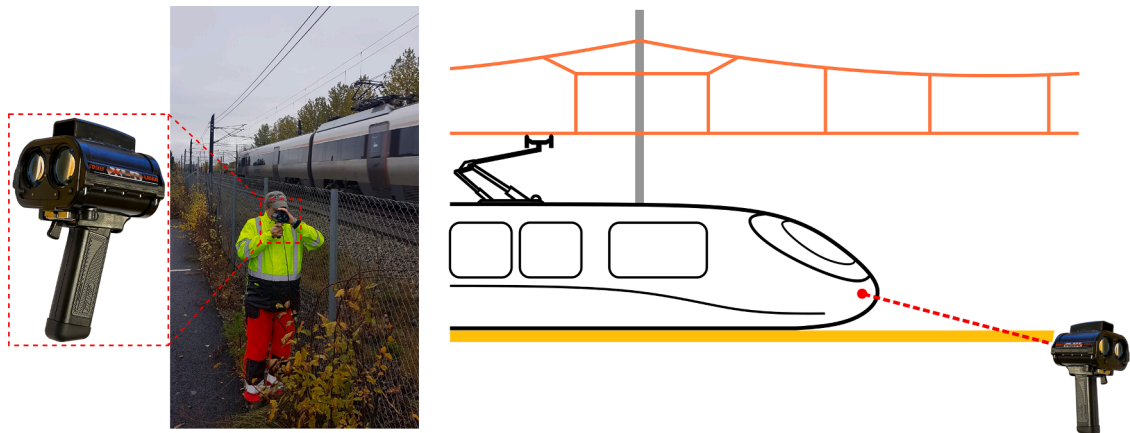


Fig. 10. Measuring train speeds by using a LiDAR device. Photography: Tengjiao Jiang/NTNU.

4. Data processing and vibration analysis

This section primarily focuses on the post-processing of the recorded image sequences, investigates the unsynchronised vibration of two contact wires and performs the spectral analysis of the post-passage response.

4.1. Displacement acquisition via post-image processing

Eleven single- and two double-pantograph train passages were recorded in total from the field tests. Image sequences were measured up to 300 s (60000 frames) for each train passage. The image sequence started before train arrival at the measured span and ended when catenary wire vibration ceased.

The image sequences were processed with the line-tracking technique mentioned in Section 2.3, and some examples of the image-processing result are shown in Fig. 11. The yellow dashed lines indicate the detected catenary wires, and the red points indicate the tracking points. $t = t_0 + i \cdot \Delta t$, where t is the time moment for each image, t_0 is the time of the first image, i is the image serial number and Δt is the time interval of 0.005 s.

In this case, each image was defined with three searching columns encompassing three tracking points of each contact wire. The shooting areas of the two cameras contained a common area. Thus, after ignoring two repeated tracking points in the common shooting area, there were ten independent tracking points for two contact wires. The region of interest (ROI) is built to reduce the searching region and improve image processing efficiency. After post-image processing, the displacement response of two wires was obtained in subpixels. It should be noted that panhead would block small sections of contact wires at contact points. However, this problem does not interrupt the wire identification and point tracking. The reason is that the image width is wide enough to ensure the panhead does not entirely block the sight of the wires, which makes the algorithm successfully identify the wires. Then, the tracking points are selected on the identified centerline of the wires, as shown in Fig. 11, which ensures the tracking points are tracked continuously even if the panhead blocks the tracking points.

The scale factor is essential to convert displacement from pixels into physical units (e.g., millimetres). A pinhole camera calibration model [20] was used to estimate the scale factor in this study. The scale factor depends on various parameters, including the image coordinates of the tracking points and centre point of the image plane, the physical pixel size, the camera pitch angle, the focal length f of the optical lens, and the distance from the optical centre to the object. Except for the contact-wire distance D_w and pitch angle θ measured in the field (mentioned in Section 2.2), the other parameters are known and related to the adopted camera and optical lens.

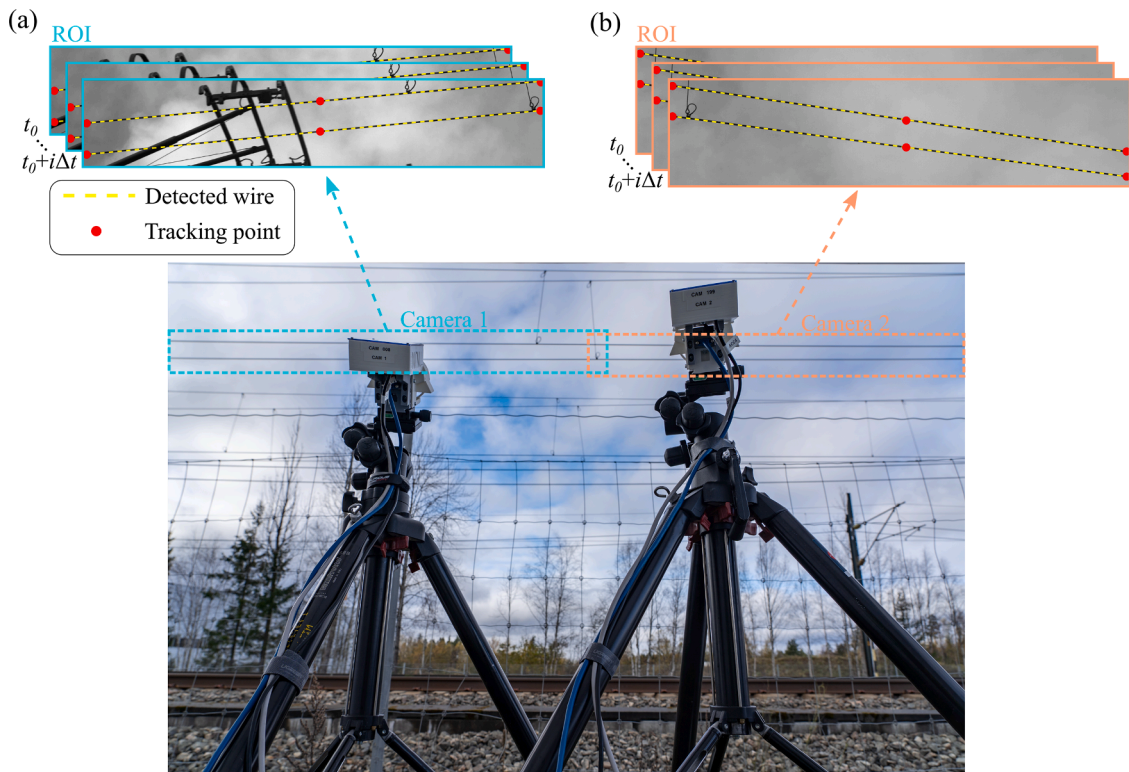


Fig. 11. Line-tracking image processing. The detected contact wires and tracking points of (a) camera 1 and (b) camera 2.

4.2. Uplift response under single-pantograph train passage

The uplift response of the first and second contact wires is shown in Fig. 12 under a single-pantograph train passage. The grey and orange regions indicate the times when the pantograph passes the measured overlap span and camera shooting area, respectively.

Fig. 12 reveals the unsynchronised vibration of two contact wires. The first contact wire reaches its maximum uplift value, around 41.7 mm, before the pantograph arrives at the static crossing location. However, the second contact wire reaches its maximum uplift value, around 51.9 mm, after the pantograph passes the static crossing location.

The maximum uplift of the second contact wire is larger than that of the first contact wire. It should also be noted that the first trough (-27.0 mm) of the first contact wire, after the maximum uplift, is much lower than that of the second wire (-10.8 mm).

After the pantograph passes the measured overlap span, the first wire exhibits free vibration, and the amplitude decays. It is further analysed in Section 5.2 to determine the distance before the static crossing location where a single pantograph interacts with the second wire.

4.3. Uplift response under double-pantograph train passage

Fig. 13 shows the uplift response under the double-pantograph passage, which is compared to that under the single-pantograph passage. Naturally, the front pantograph causes the first uplift peaks of the first and second contact wires, and the rear pantograph causes the second peaks. Similar to the single-pantograph passage, the maximum uplift of the second contact wire (53.0 and 48.3 mm, respectively) is larger than that of the first contact wire (39.7 and 34.7 mm, respectively) for both the front and rear pantographs.

Passage of the front pantograph causes a large vibration in the contact wires, which could affect the contact quality of the rear pantograph. The maximum uplift when the rear pantograph passes (53.0 mm) is larger than that when the front pantograph passes (48.3 mm). The front and rear pantographs both interact with the second wire before reaching the static crossing point, which is further studied in Section 5.3.

4.4. Spectral analysis

Spectral analysis [40] of the first and second contact wires perform on their post-passage displacement response. The post-passage response is after the passage of the pantograph, which is mainly caused by the excitation of the pantograph uplift, and the following decaying response is dominated by the fundamental frequencies.

Fig. 14 shows an example of train passage segments, divided into three parts, including pre-passage, passing the span and post-passage. The pre-passage is before the pantograph passage at the measured span, and the catenary wires are excited by the forward wave causing oscillations. The passing segment is the pantograph passing through the measured span from one steady arm to another.

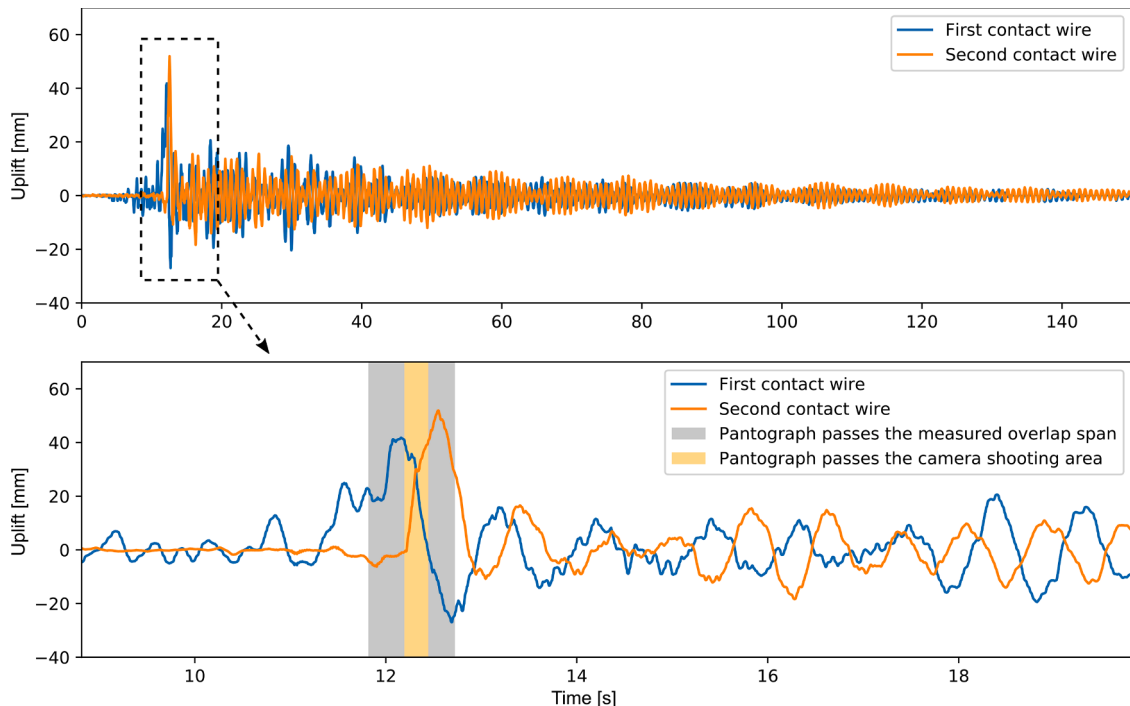


Fig. 12. Uplift response of the first and second contact wires under single-pantograph train passage.

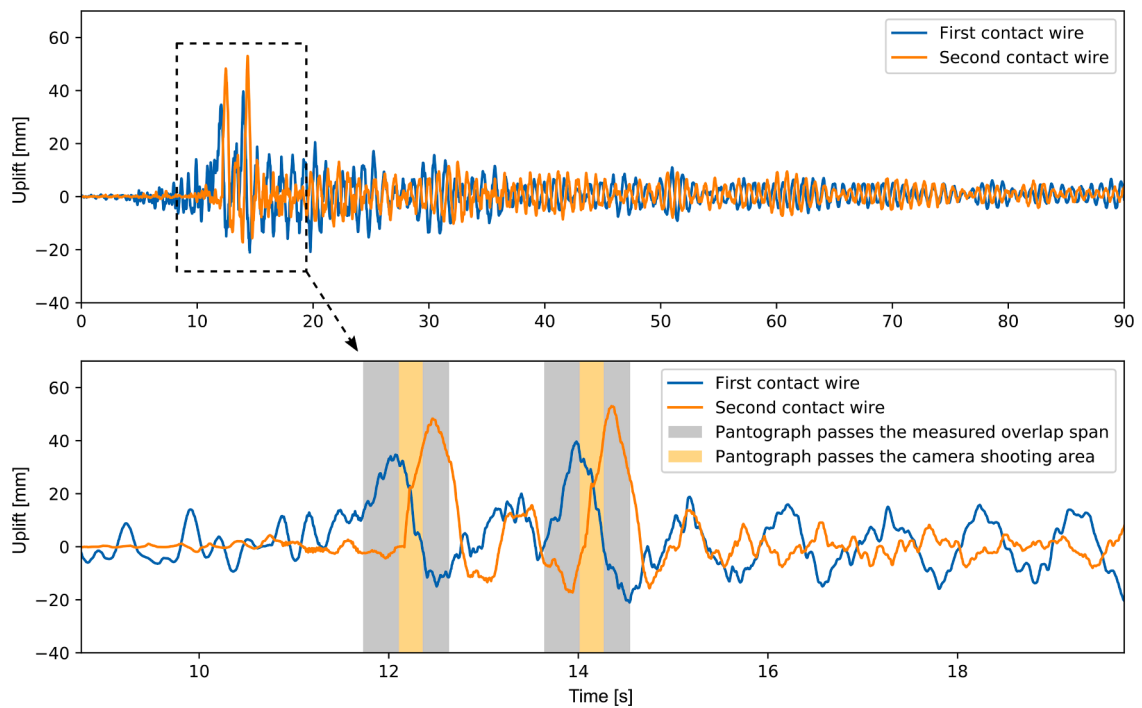


Fig. 13. Uplift response of the contact wires under double-pantograph train passage.

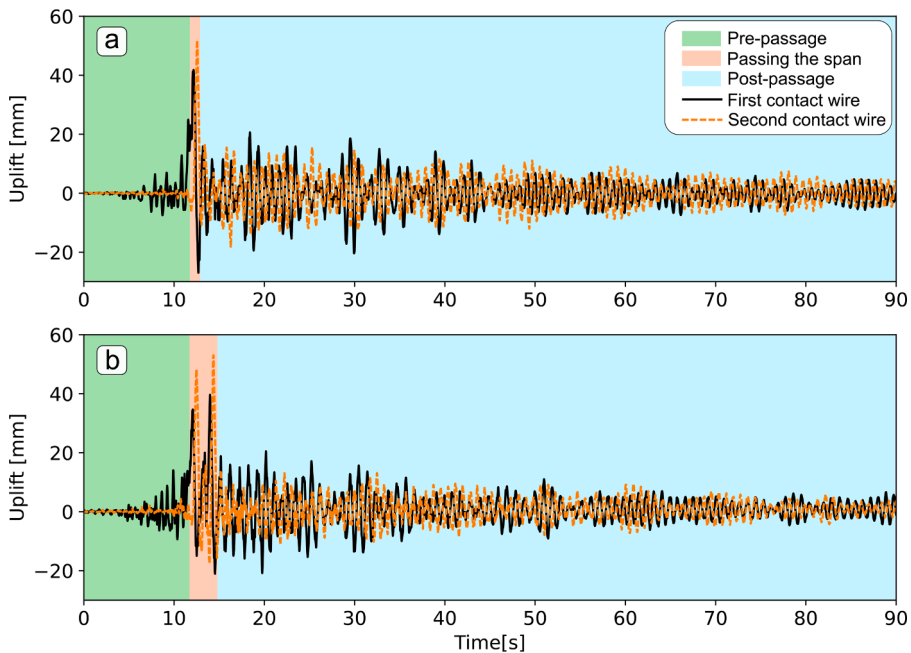


Fig. 14. An example of train passage segments: pre-passage, passing the span and post-passage. (a) Single-pantograph train passage; (b) double-pantograph train passage.

The spectral analysis results of single- and double-pantograph train passages are shown in Fig. 15. One interesting finding is the dominant modal frequencies of the first contact wire (i.e., with high amplitude) are shifted from 1.27 Hz in Fig. 15 (a) to 0.98 Hz and 1.16 Hz in Fig. 15 (b) under the double-pantograph train passage. The dominant modal frequencies of the second contact wire remain almost unchanged, whether under a single- or double-pantograph.

To verify the data was not contaminated, multiple tests are performed and finally obtain the same phenomenon of the shifted

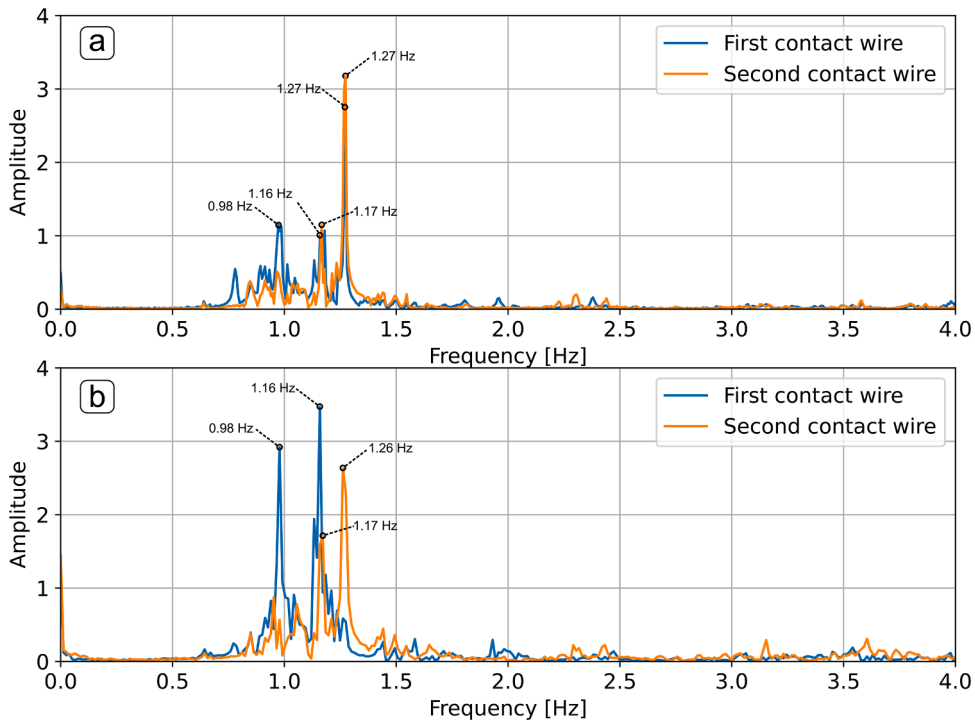


Fig. 15. Spectral analysis of post-passage response. (a) Single-pantograph train passage; (b) double-pantograph train passage.

dominant modal frequencies. One explanation is that the double-pantograph passage has a different excitation way, which can excite the different modal responses of the catenary system at the overlap span. The first contact wire is at the end of the first catenary section, which is close to the wave reflector source. However, the second contact wire is at the start of the second catenary section, and the wave propagation occurs after the pantograph passage. Thus, the first wire is more susceptible to wave propagation than the second wire, also shown in Fig. 14. The maximum uplift of the first wire (41.7 mm) when the pantograph passes through is smaller than that of the second wire (51.9 mm) in Fig. 14 (a). However, in post-passage, the vibration amplitude of the first wire is generally larger than that of the second wire for 15 ~ 40 seconds. This phenomenon is more evident under the double-pantograph passage in Fig. 14 (b). Thus, the first wire is more likely to exhibit different modal responses under the dual impact of double-pantograph excitation and wave propagation.

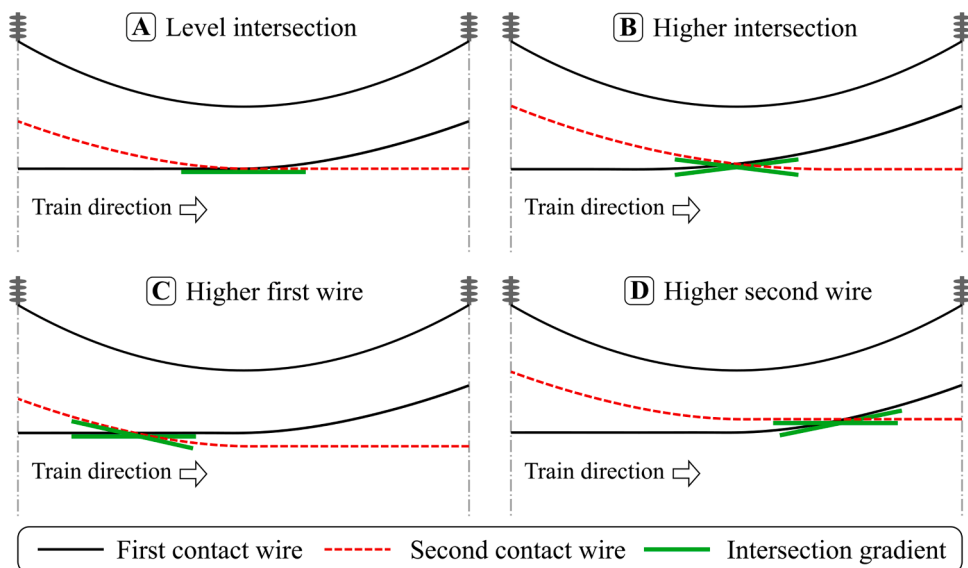


Fig. 16. Intersection configuration types of the contact wires in the overlap sections.

5. Assessment of pantograph-catenary interaction

This section aims to study the pantograph-catenary interaction in the overlap section by using the method proposed in Section 2. The spatial motion path of the crossing point illustrates the contact situations under single- and double-pantograph train passages in Sections 5.2 and 5.3, respectively. The correlation study between the train speed, transition distance and contact force is performed in Section 5.4.

5.1. Contact wire configuration and transition segment

The intersection configuration of the contact wires has been classified into four types in the literature [21,23], as shown in Fig. 16. Type A is a level intersection where the intersection gradient is level with the contact wire, and type B is a higher intersection, i.e., the crossing point is higher than the contact wire height. Type C is the higher first wire type, i.e., the height of the first contact wire is higher than that of the second wire, and the opposite applies to type D.

In construction, the static crossing point is either raised or lowered as part of the design geometry. To reduce the transition distance when the pantograph contacts both contact wires under type A, the crossing point is elevated 40 to 60 mm above the contact wire height, rendering the type B design geometry.

The literature [23] has indicated that wire wear under types B and C exceeds that under types A and D. In Norway, most railways are two-direction tracks, i.e., trains run along with both directions on a single track. Only a few railway tracks in Oslo are one-directional. Catenary type D is only suitable for one-direction tracks. Moreover, two-directional running results in more wear under type D, similar to type C. Due to the shortcomings of the long transition distance of type A, type B has become the conventional design geometry for two-direction railway tracks in Norway.

For the clarity of the following study, some definitions in this study are set and illustrated first. A transition segment, where pantographs transition between adjacent catenary sections, is a section between initial and end contact points, as shown in Fig. 17. A

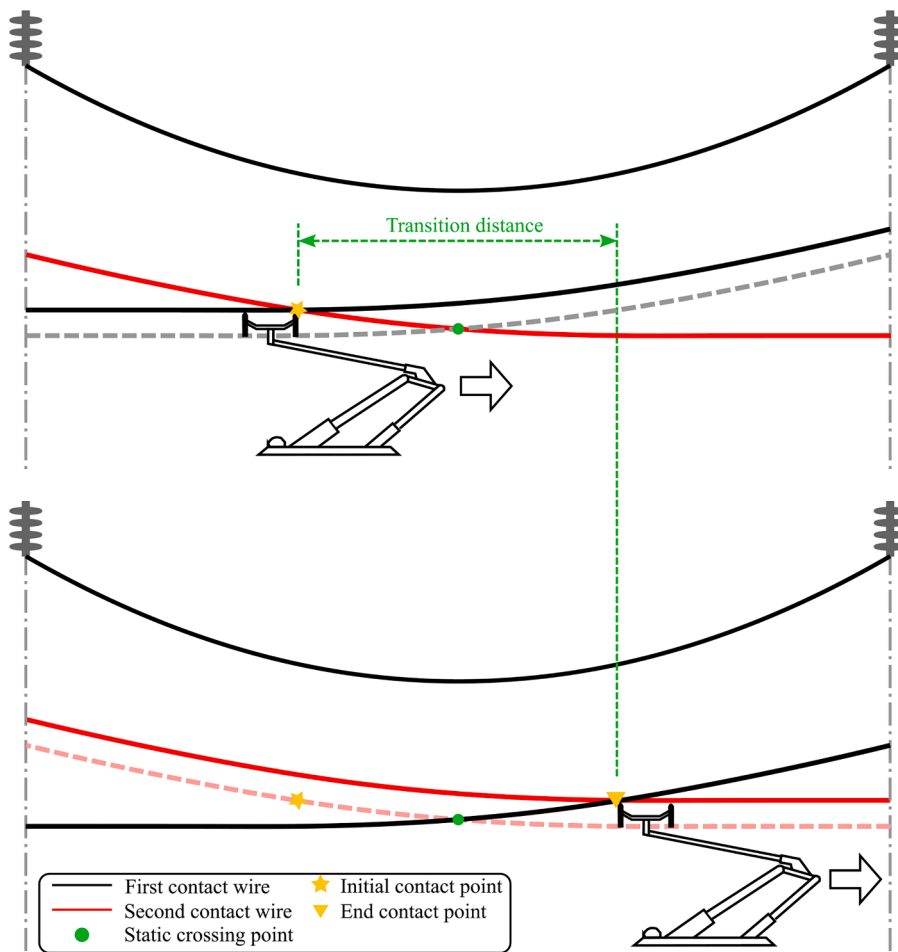
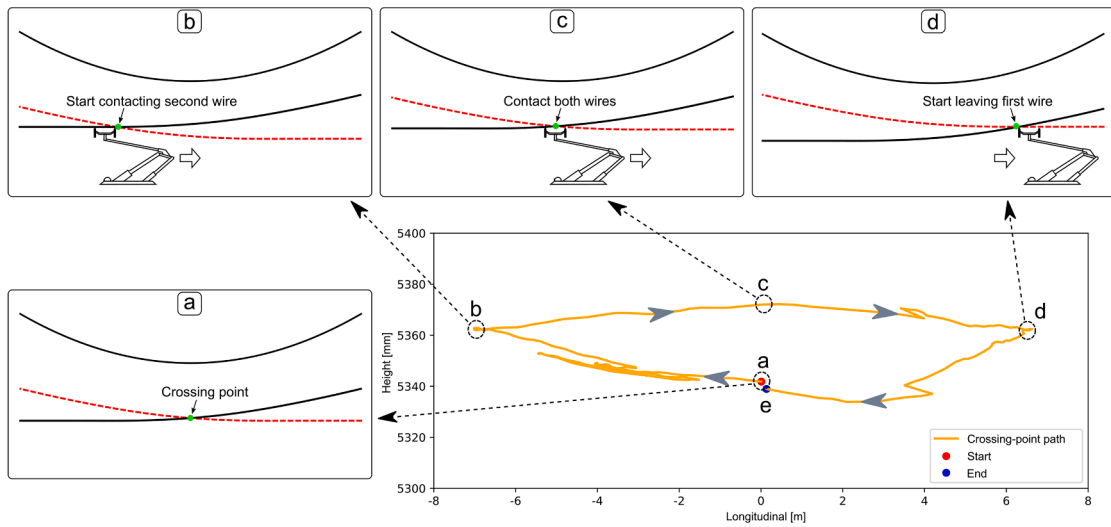


Fig. 17. Transition segment within the overlap span.

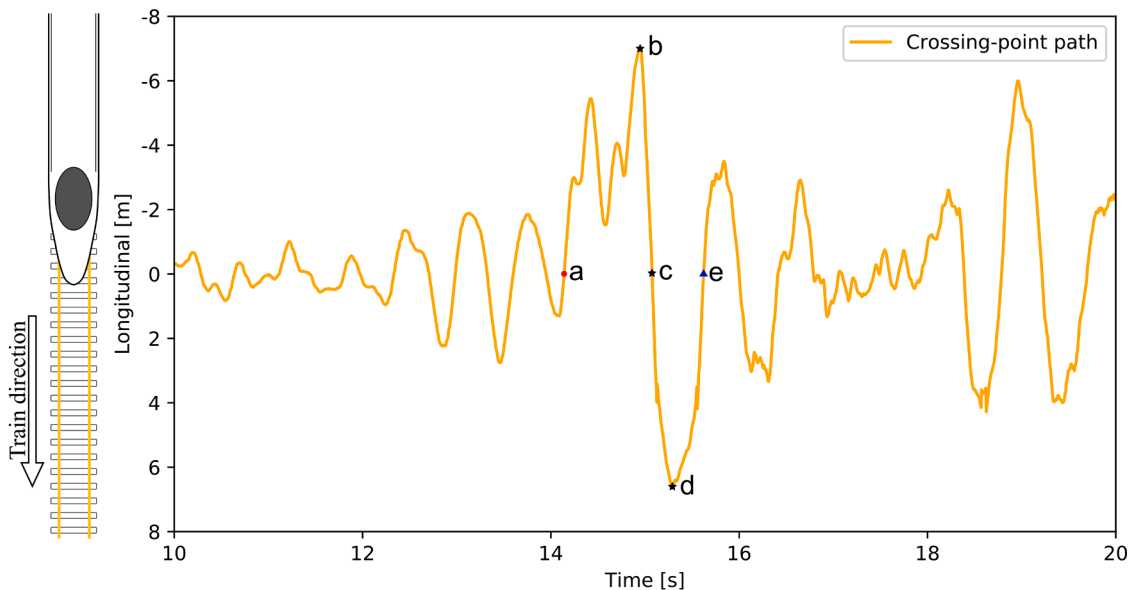
transition distance is the distance of the transition segment where the pantograph remains in contact with both wires for a certain distance until leaving the first contact wire. The initial contact point is a point where the pantograph starts to contact the second contact wire, and the end contact point is a point where the pantograph leaves the first contact wire. A static crossing point is the intersection of the two static contact wires on the vertical plane.

5.2. Dynamic crossing point under single-pantograph train passage

Under single-pantograph train passage, the spatial path of the crossing point is visualised to reveal the pantograph-catenary interaction at the overlap section in detail. A segment of the motion path and corresponding situations of the pantograph-catenary interaction are shown in Fig. 18 (a). The x-axis is the longitudinal distance from the camera setup location along the rail. The y-axis is the height from the rail along the vertical direction. An illustration of the longitudinal distance and height is shown in Fig. 19. Fig. 18 (b) shows the motion path of the dynamic crossing point in a time series from a top view. The y-axis is the longitudinal distance, and the train running direction is from top to bottom. The whole motion path can be interpreted as follows:



(a) Motion path of the dynamic crossing point and its corresponding situations of pantograph-catenary interaction.



(b) Motion path of the dynamic crossing point in a time series from a top view.

Fig. 18. Investigation of pantograph-catenary interaction in the transition segment under single-pantograph train passage.

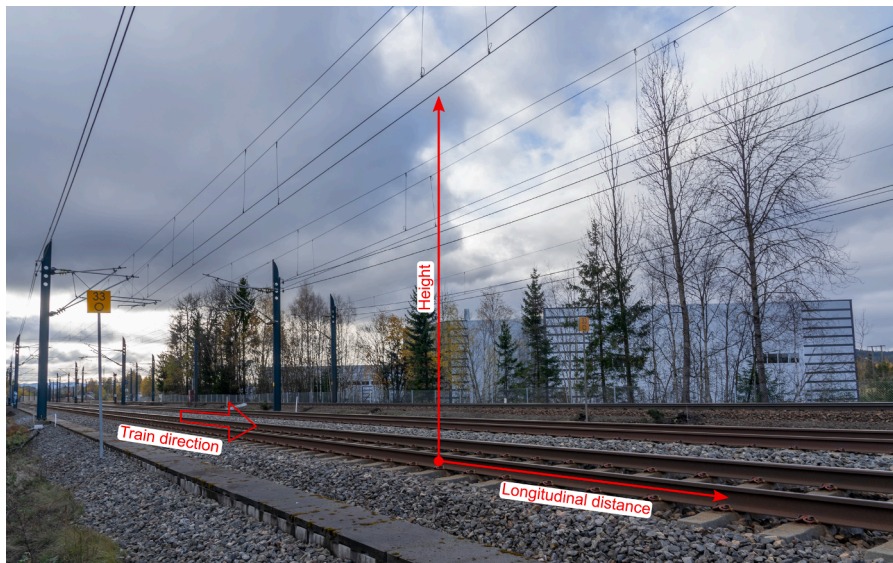


Fig. 19. Illustration of the longitudinal distance and height.

- The red point, a, i.e., the starting point, indicates when the pantograph reaches the previous span before the measured span.
- As the pantograph approaches, the first contact wire starts to vibrate, and the uplift increases. This moves the crossing point towards the train.
- When the pantograph starts to contact the second wire, the crossing point now occurs at point b (the initial contact point).
- The pantograph then comes into contact with both wires within the transition section, and the crossing point follows the pantograph motion to point c at the midspan.
- The pantograph remains in contact with both wires until point d, when the first wire descends and the second wire is lifted. Point d is the moment when the pantograph loses contact with the first wire, i.e., the end contact point.
- Thereafter, the pantograph successfully transitions to the consecutive catenary section. Without the pantograph contact force, the vibration in the first wire decays, and the crossing point moves to point e.

The results show that the pantograph starts to contact the second wire at the initial contact point b, where the intersection gradient is high, similar to type C in Fig. 16. Thus, this would produce a large impulse instead of a smooth contact between the pantograph and the second wire. The literature [23] proves type C results in high wear of the contact wires. Through numerical simulations, Gregori et al. [10] also found that the peak force occurs when the pantograph starts interacting with the second wire some metres before reaching the static crossing point.

Thus, the distant initial contact point with a high intersection gradient could be the reason why the maximum contact force appears at the overlap span. The impulse generally increases contact wire wear and may induce contact loss and arcing. The reason is that the impulse would cause the second contact wire to bounce, resulting in a contact loss and a temporary air gap. The electrons shooting through the gap turn the air into plasma and break down the air, which causes arcing. This study also recorded arcing by the camera at an initial contact point with a distance of 6.72 m before the static crossing point, as shown in Fig. 20, which supports the above statement. The correlation between the transition distance and the peak contact force is also studied in Section 5.4 to prove the above statement.

5.3. Dynamic crossing point under double-pantograph train passage

The motion path of the dynamic crossing point was also studied under the double-pantograph passages to determine why the rear pantograph attains a higher probability of contact loss and arcing in overlap spans. Two segments of the motion path of the dynamic crossing during the front and rear pantographs passing are shown in Fig. 21 (a), represented as a solid orange line and a dashed blue line, respectively. Fig. 21 (b) shows the motion path of the dynamic crossing point from a top view in a time series.

The two motion paths start from points a_1 and a_2 , which are close to the static crossing point location. These dynamic crossing points move to the initial contact points b_1 and b_2 , respectively, while both pantographs start interacting with the second contact wire. However, for the rear pantograph, point b_2 moves further along the longitudinal direction towards the span pole than does point b_1 (representing the front pantograph). This may cause a higher intersection gradient of the contact wires for the rear pantograph, as shown in Fig. 22.

The front and rear pantographs stay in contact with both wires, similar to the single pantograph. The crossing points b_1 and b_2 follow the pantograph movement to points c_1 and c_2 , respectively. The uplift of the rear pantograph is larger than that of the front

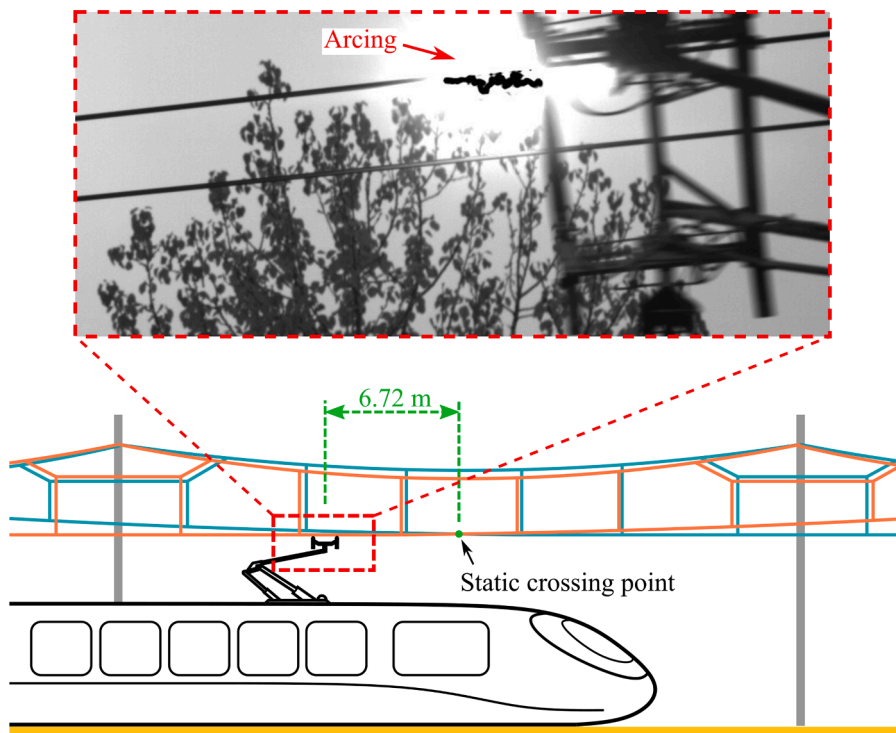


Fig. 20. Arcing occurred at the initial contact point during the measurement. Photography: Tengjiao Jiang/NTNU.

pantograph.

The front and rear pantographs stay in contact with both wires until they reach the points d_1 and d_2 , respectively. Points d_1 and d_2 are close in height and longitudinal location, in contrast to points b_1 and b_2 which greatly differ along the longitudinal direction. Points d_1 and d_2 are the moments when the pantographs lose contact with the first wire, i.e., the end contact points. Finally, the crossing points move to e_1 and e_2 , respectively.

Fig. 21 (b) shows that the crossing point is already in motion before the pantograph arrives, which is caused by wave propagation. The increased motion magnitude of the crossing point in Fig. 21 (b) from 8 to 10 s is caused by the increased magnitude of wave propagation as the pantograph gets closer. The pantograph lifts the first contact wire around 40 mm, making crossing points from a_1 move to b_1 .

In summary, the rear pantograph achieves a greater longitudinal distance and intersection gradient (point b_2) and a higher uplift (point c_2) than those of the front pantograph. One explanation is the unsynchronised vibration of two contact wires, observed in Sections 4.2 and 4.3, would result in worse contact of the rear pantograph. The rear pantograph enters the catenary system that is already in motion due to the front pantograph. Thus, the rear pantograph could experience a more severe impulse and a higher risk of contact loss and arcing within the overlap span than those experienced by the front pantograph. The more severe impulse could induce the rear pantograph to attain a higher contact force. The higher contact force of the rear pantograph is also investigated in Section 5.4.

5.4. The correlation study between the train speed, transition distance and contact force

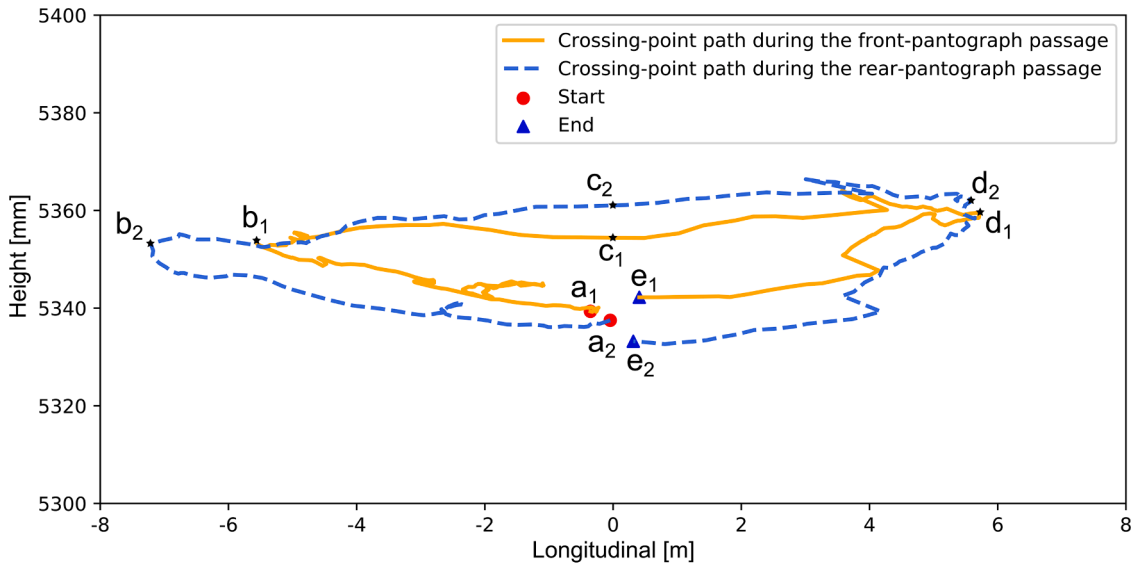
This section aims to study the correlation between the train speed, the transition distance and the contact force. A higher train speed imposes a negative effect on the contact quality of pantograph-catenary interaction [41,42].

The transition distance was estimated as 13.4 m via a numerical simulation of a single pantograph operating at 300 km/h in the literature [9]. However, no field measurement of the transition distance in existing overlap spans has been found in the literature.

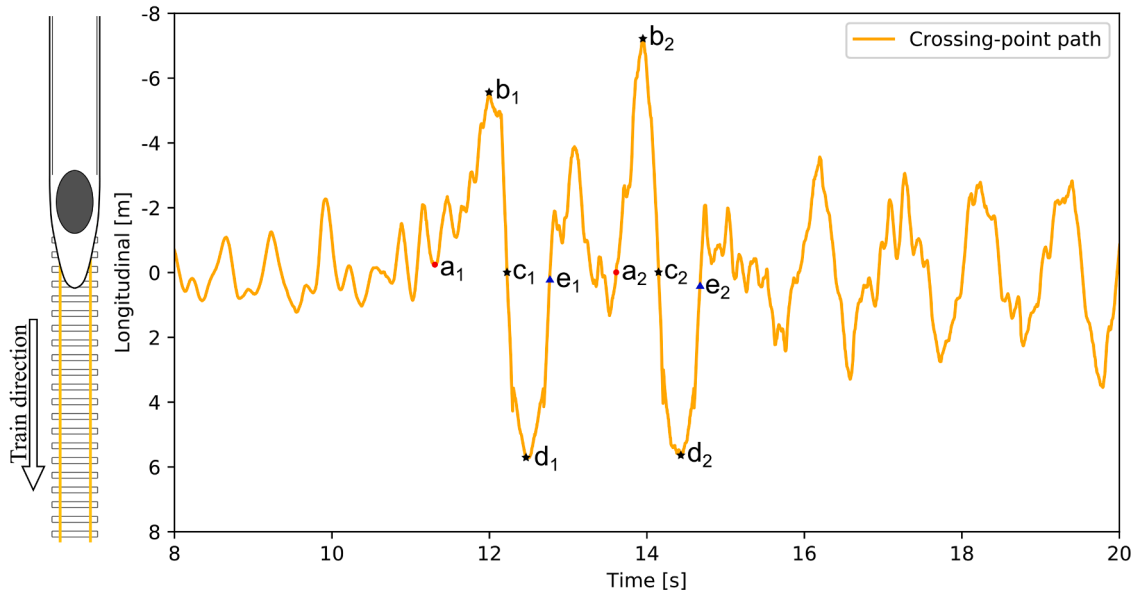
The transition distance of eleven train passages is estimated based on the dynamic crossing point spatial path, i.e., the distance between the initial and end contact points in Sections 5.2 and 5.3. Fig. 23 (a) shows the transition distances and corresponding train speeds. The result shows that the transition distance exhibits an increasing tendency with increasing train speed. The measured transition distances are approximately 14 and 10 m at train speeds of 210 and 179 km/h, respectively. This variation clearly shows a significant train speed dependency.

According to Newton's second law in Eq. (5), the acceleration a of the contact wire can be used to judge the magnitude F of the contact force because the mass m is always the same for every train passage.

$$F = m \cdot a \quad (5)$$



(a) Motion path of the dynamic crossing point under double-pantograph train passage.



(b) Motion path of the dynamic crossing point in a time series from a top view.

Fig. 21. Investigation of pantograph-catenary interaction in the transition segment under double-pantograph train passage.

where F is the contact force between the pantograph and the contact wire, and m is the mass of the contact wire.

Section 5.2 and 5.3 find that the longer transition distance results in a larger intersection gradient of two contact wires, and the pantograph is more likely to have a larger impulse with the second contact wire. To certify this finding, the relationship between the transition distance and maximum acceleration of the second contact wire is studied in Fig. 23 (b). The acceleration was estimated using a second-time derivative from the displacement data obtained from the vision-based system.

The result shows the maximum acceleration increases with the transition distance. The maximum acceleration happens when the pantograph contacts the second contact wire (i.e., at the initial contact point). This finding demonstrates the peak contact force has a strong correlation with the transition distance. The rear pantograph with a longer transition distance would have a higher contact force.

It can be deduced that the higher static preload of pantographs (mean value of contact force) would also result in an earlier contact between the panhead and the second contact wire and a larger transition distance. More field tests of correlation between the static preload and the transition distance will perform in the future.

In summary, the transition distance exhibits an increasing tendency with increasing train speed. The longer transition distance

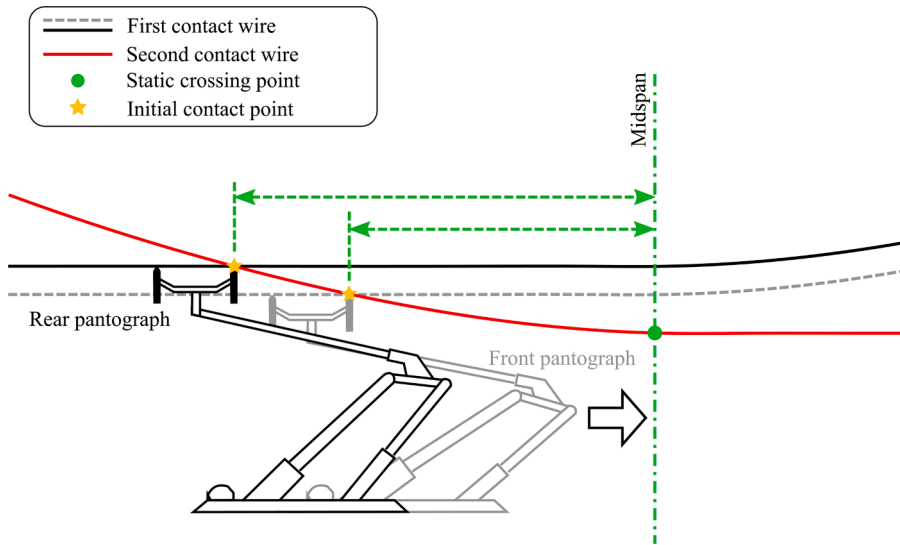


Fig. 22. Greater longitudinal distance and intersection gradient for the rear pantograph.

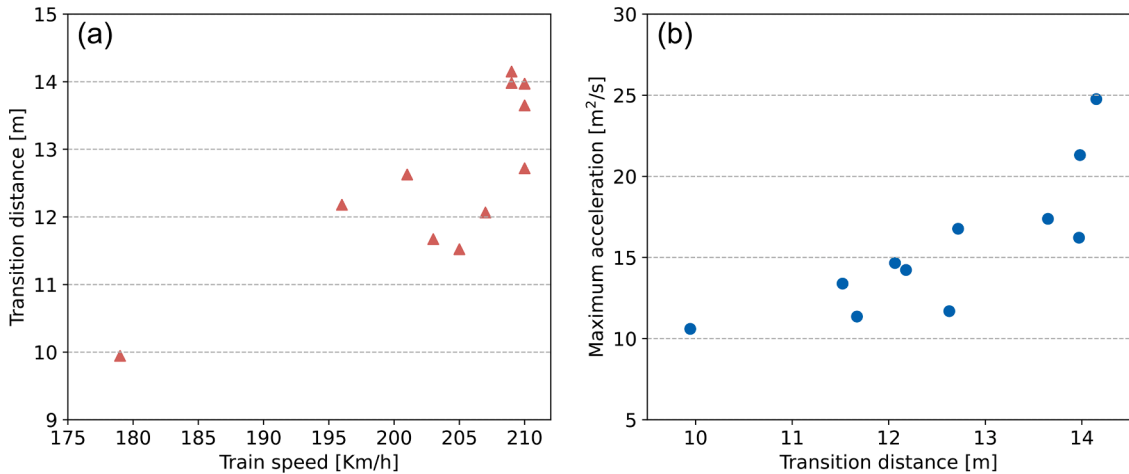


Fig. 23. Relationship between the train speed, transition distance and maximum acceleration.

could result in a higher peak contact force.

6. Conclusion

This experimental study under regular traffic conditions evaluates the dynamic behaviour of pantograph-catenary interaction at an existing overlap span. A novel overlap measuring method was proposed and implemented at a five-span overlap. Image sequences of eleven single- and two double-pantograph train passages were acquired with the VIBLITE, and a hand-held gun-type LiDAR was employed to measure the train speed. The spatial motion paths of two contact wires were obtained, and their dynamic crossing point was estimated and compared in detail under single- and double-pantograph train passages. This investigation studied the correlation between train speed, the transition distance and the contact force. The main conclusions are summarised as follows:

- The successful application of the optical-based measuring method proves its feasibility in studying pantograph-catenary interaction and transition in catenary overlap spans.
- The unsynchronised vibration of two contact wires has been found in this study. The first contact wire exhibits different modal responses under single- and double-pantograph train passages. A clear difference in maximum uplift and transition distance is observed between single and double pantographs.
- This study investigated the dynamic effects rendering high contact forces, contact loss and arcing at overlap spans. The results reveal that the pantograph contacts the second wire at a certain distance before reaching the static crossing point. The longer

distance results in a larger intersection gradient of two contact wires, and the pantograph is prone to have a larger impulse with the second contact wire. This phenomenon results in contact loss and arcing at the initial contact point, where peak contact force occurs. Because of the longer transition distance, the rear pantograph causes a more severe dynamic interaction and higher contact force with the catenary system.

- This study estimated the transition distance successfully and found that the peak contact force, the transition distance and the train speed have a strong positive correlation. The transition distance exhibits an increasing tendency with increasing train speed. The longer transition distance could result in a higher peak contact force.

Declaration of Competing Interest

The authors declare that they have no known competing financial interests or personal relationships that could have appeared to influence the work reported in this paper.

Acknowledgements

The research presented in this article constituted part of the PhD research of Tengjiao Jiang and was financed by the China Scholarship Council and the Norwegian Railway Directorate. Norske tog AS and Flytoget AS are acknowledged for providing the train photos.

References

- [1] J. Pombo, J. Ambrósio, M. Pereira, F. Rauter, A. Collina, A. Facchinetti, Influence of the aerodynamic forces on the pantograph–catenary system for high-speed trains, *Veh. Syst. Dyn.* 47 (2009) 1327–1347.
- [2] Y. Song, P. Antunes, J. Pombo, Z. Liu, A methodology to study high-speed pantograph–catenary interaction with realistic contact wire irregularities, *Mech Mach Theory* (2020) 103940.
- [3] B. Blanco, I. Errandonea, S. Beltrán, S. Arrizabalaga, U. Alvarado, Panhead accelerations-based methodology for monitoring the stagger in overhead contact line systems, *Mech. Mach. Theory* 171 (2022), 104742.
- [4] P. Návík, S. Derosa, A. Rønquist, Development of an index for quantification of structural dynamic response in a railway catenary section, *Eng. Struct.* 222 (2020), 111154.
- [5] M. Tan, N. Zhou, J. Wang, D. Zou, W. Zhang, G. Mei, A real-time impact detection and diagnosis system of catenary using measured strains by fibre Bragg grating sensors, *Veh. Syst. Dyn.* 57 (2019) 1924–1946.
- [6] Y. Song, Z. Wang, Z. Liu, R. Wang, A spatial coupling model to study dynamic performance of pantograph–catenary with vehicle–track excitation, *Mech. Syst. Signal Process.* 151 (2021), 107336.
- [7] I. Aydın, A new approach based on firefly algorithm for vision-based railway overhead inspection system, *Measurement* 74 (2015) 43–55.
- [8] Y. Song, T. Jiang, A. Rønquist, P. Návík, G. Frøseth, The Effects of Spatially Distributed Damping on the Contact Force in Railway Pantograph–Catenary Interactions, *IEEE Trans. Instrum. Meas.* 70 (2021) 1–10.
- [9] S. Gregori, J. Gil, M. Tur, J.E. Tarancón, F.J. Fuenmayor, Analysis of the overlap section in a high-speed railway catenary by means of numerical simulations, *Eng. Struct.* 221 (2020), 110963.
- [10] F. Vesali, H. Molatefi, M.A. Rezvani, B. Moaveni, M. Hecht, New control approaches to improve contact quality in the conventional spans and overlap section in a high-speed catenary system, *Proc. Inst. Mech. Eng. Part F: J. Rail Rapid Transit* 233 (2019) 988–999.
- [11] F. Kiessling, R. Puschmann, A. Schmieder, E. Schneider, *Contact lines for electric railways: planning, design, implementation, maintenance*, John Wiley & Sons, 2018, 2 ed.
- [12] P. Antunes, J. Ambrósio, J. Pombo, A. Facchinetti, A new methodology to study the pantograph–catenary dynamics in curved railway tracks, *Veh. Syst. Dyn.* 58 (2020) 425–452.
- [13] J.-P. Massat, C. Laurent, J.-P. Bianchi, E. Balmès, Pantograph catenary dynamic optimisation based on advanced multibody and finite element co-simulation tools, *Veh. Syst. Dyn.* 52 (2014) 338–354.
- [14] J.R. Jiménez-Octavio, M. Such, A. Carnicero, O. Lopez-García, Validation of simulation approaches for catenary–pantograph dynamics, in: B.H.V Topping, M Papadarakakis (Eds.), *Proceedings of the Ninth International Conference on Computational Structures Technology*, Civil-Comp Press, Stirlingshire, UK, 2008.
- [15] P. Zdziebko, A. Martowicz, T. Uhl, Multi-domain approach to modeling pantograph–catenary interaction, *Eksplotacja i Niezawodność-Maintenance and Reliability* 24 (2022) 130–139.
- [16] Y. Song, A. Rønquist, T. Jiang, P. Návík, Identification of short-wavelength contact wire irregularities in electrified railway pantograph–catenary system, *Mech. Mach. Theory* 162 (2021), 104338.
- [17] Y. Song, T. Jiang, P. Návík, A. Rønquist, Geometry deviation effects of railway catenaries on pantograph–catenary interaction: a case study in Norwegian Railway System, *Railw. Eng. Sci.* 29 (2021) 350–361.
- [18] Z. Xu, Y. Song, Z. Liu, Effective Measures to Improve Current Collection Quality for Double Pantographs and Catenary Based on Wave Propagation Analysis, *IEEE Trans. Veh. Technol.* (2020) 1, 1–.
- [19] T. Jiang, G.T. Frøseth, A. Rønquist, E. Fagerholt, A robust line-tracking photogrammetry method for uplift measurements of railway catenary systems in noisy backgrounds, *Mech. Syst. Signal Process.* 144 (2020), 106888.
- [20] T. Jiang, A. Rønquist, Y. Song, G.T. Frøseth, P. Návík, A detailed investigation of uplift and damping of a railway catenary span in traffic using a vision-based line-tracking system, *J. Sound Vib.* (2022), 116875.
- [21] M. Shimizu, Y. Fujii, Improvement of Structure of Contact Wire on Overlap Sections of Shinkansen, *Quarterly Report of RTRI* 41 (2000) 159–162.
- [22] P. Harèll, L. Drugge, M. Reijm, Study of Critical Sections in Catenary Systems During Multiple Pantograph Operation, *Proc. Inst. Mech. Eng. Part F: J. Rail Rapid Transit* 219 (2005) 203–211.
- [23] T. Kuraoka, I. Ideno, Research on Reduction of Wear of Contact Wires in Overlap Sections, *JR East Technical Review* (2012).
- [24] C.-Z. Dong, S. Bas, F.N. Catbas, A portable monitoring approach using cameras and computer vision for bridge load rating in smart cities, *J. Civ. Struct. Health Monit.* 10 (2020) 1001–1021.
- [25] C.-Z. Dong, F.N. Catbas, A review of computer vision–based structural health monitoring at local and global levels, *Struct. Health Monit.* (2020).
- [26] T. Jiang, L. Tang, Z. Zhou, Study on Application of Close-Range Photogrammetric 3D Reconstruction in Structural Tests, *Res. Explor. Lab* 35 (2016) 26–29.
- [27] G. Deng, Z. Zhou, S. Shao, X. Chu, P. Du, Novel approach to extract dense full-field dynamic parameters of large-scale bridges using spatial sequence video, *J. Civ. Eng. Manag.* 27 (2021) 617–636.
- [28] T. Wu, L. Tang, P. Du, N. Liu, Z. Zhou, X. Qi, Non-contact measurement method of beam vibration with laser stripe tracking based on tilt photography, *Measurement* 187 (2022), 110314.

- [29] K. Zaletelj, V. Agrež, J. Slavič, R. Petkovšek, M. Boltežar, Laser-light speckle formation for deflection-shape identification using digital image correlation, *Mech. Syst. Signal Process.* 161 (2021), 107899.
- [30] D. Gorjup, J. Slavič, A. Babnik, M. Boltežar, Still-camera multiview Spectral Optical Flow Imaging for 3D operating-deflection-shape identification, *Mech. Syst. Signal Process.* 152 (2021), 107456.
- [31] Y.F. Xu, A photogrammetry-based experimental modal analysis method by tracking visible laser spots, *Measurement* 151 (2020), 106963.
- [32] M. Southwick, Z. Mao, C. Niezrecki, A Complex Convolution Kernel-Based Optical Displacement Sensor, *IEEE Sens. J.* 20 (2020) 9753–9762.
- [33] Y. Gu, P. Lan, Y. Cui, K. Li, Z. Yu, Dynamic interaction between the transmission wire and cross-frame, *Mech. Mach. Theory* 155 (2021) 104068.
- [34] Y. Chen, D.T. Griffith, Experimental and numerical investigation of the structural dynamic characteristics for both surfaces of a wind turbine blade, *J. Vib. Control* (2022), 10775463221097470.
- [35] L. Rui, E. Zappa, A. Collina, Vision-based measurement of crack generation and evolution during static testing of concrete sleepers, *Eng. Fract. Mech.* 224 (2020), 106715.
- [36] P. Urda, J.F. Aceituno, S. Muñoz, J.L. Escalona, Artificial neural networks applied to the measurement of lateral wheel-rail contact force: A comparison with a harmonic cancellation method, *Mech. Mach. Theory* 153 (2020), 103968.
- [37] T. Jiang, G.T. Frøseth, A. Rønquist, E. Fagerholt, A vision-based line-tracking technique, *Zenodo* (2020).
- [38] Jernbaneverket, *Mekanisk systembeskrivelse av kontaktledningsanlegg*, 2019.
- [39] Basler AG, *Basler Product Documentation*, 2018.
- [40] Y. Ye, B. Zhu, P. Huang, B. Peng, OORNet: A deep learning model for on-board condition monitoring and fault diagnosis of out-of-round wheels of high-speed trains, *Measurement* 199 (111268) (2022).
- [41] Y.H. Cho, K. Lee, Y. Park, B. Kang, K.-n. Kim, Influence of contact wire pre-sag on the dynamics of pantograph–railway catenary, *Int. J. Mech. Sci.* 52 (2010) 1471–1490.
- [42] A. Collina, S. Bruni, Numerical Simulation of Pantograph-Overhead Equipment Interaction, *Veh. Syst. Dyn.* 38 (2002) 261–291.